

# 3D/2D Vessel Registration Based on Monte Carlo Tree Search and Manifold Regularization

Jianjun Zhu<sup>ID</sup>, Member, IEEE, Cheng Wang, Member, IEEE, Yi Zhang, Meixiao Zhan, Wei Zhao, Sitong Teng, Ligong Lu, and Gao-Jun Teng<sup>ID</sup>

**Abstract**— The augmented intra-operative real-time imaging in vascular interventional surgery, which is generally performed by projecting preoperative computed tomography angiography images onto intraoperative digital subtraction angiography (DSA) images, can compensate for the deficiencies of DSA-based navigation, such as lack of depth information and excessive use of toxic contrast agents. 3D/2D vessel registration is the critical step in image augmentation. A 3D/2D registration method based on vessel graph matching is proposed in this study. For rigid registration, the matching of vessel graphs can be decomposed into continuous states, thus 3D/2D vascular registration is formulated as a search tree problem. The Monte Carlo tree search method is applied to find the optimal vessel matching associated with the highest rigid registration score. For nonrigid registration, we propose a novel vessel deformation model based on manifold regularization. This model incorporates the smoothness constraint

Manuscript received 19 July 2023; revised 18 November 2023; accepted 22 December 2023. Date of publication 28 December 2023; date of current version 2 May 2024. This work was supported in part by the National Natural Science Foundation of China under Grant 81827805, Grant 82130060, Grant 61821002, and Grant 92148205; in part by the National Key Research and Development Program under Grant 2018YFA0704100 and Grant 2018YFA0704104; in part by the Project funded by China Post-Doctoral Science Foundation under Grant 2021M700772; in part by the Zhuhai Industry-University-Research Collaboration Program under Grant ZH22017002210011PWC; in part by the Jiangsu Provincial Medical Innovation Center under Grant CXZX202219; in part by the Collaborative Innovation Center of Radiation Medicine of Jiangsu Higher Education Institutions, Nanjing Life Health Science and Technology Project 202205045; in part by the Jiangsu Province Science and Technology Support Project BE2023769; and in part by the Natural Science Foundation of Guangdong Province of China under Grant 2021A1515220183 and Grant 2022B1515020010. (Jianjun Zhu and Cheng Wang contributed equally to this work.) (Corresponding authors: Ligong Lu; Gao-Jun Teng.)

Jianjun Zhu is with Hanglok-Tech Company Ltd., Zhuhai, Hengqin 519030, China, and also with the Center of Interventional Radiology & Vascular Surgery, Department of Radiology, Medical School, Zhongda Hospital, Southeast University, Nanjing 210009, China (e-mail: jj.zhu@hanglok-tech.cn).

Cheng Wang and Sitong Teng are with Hanglok-Tech Company Ltd., Zhuhai, Hengqin 519030, China (e-mail: cheng.wang@hanglok-tech.cn; anna.teng@queensu.ca).

Yi Zhang and Gao-Jun Teng are with the Center of Interventional Radiology & Vascular Surgery, Department of Radiology, Medical School, Zhongda Hospital, Southeast University, Nanjing 210009, China (e-mail: yizhangcir@126.com; gjteng@vip.sina.com).

Meixiao Zhan, Wei Zhao, and Ligong Lu are with the Guangdong Provincial Key Laboratory of Tumor Interventional Diagnosis and Treatment, Zhuhai People's Hospital, Zhuhai Hospital, Jinan University, Zhuhai, Guangdong 519000, China (e-mail: zhanmeixiao1987@126.com; zhaoweismu@foxmail.com; luligong1969@jnu.edu.cn).

Digital Object Identifier 10.1109/TMI.2023.3347896

of vessel topology into the objective function. Furthermore, we derive simplified gradient formulas that enable fast registration. The proposed technique undergoes evaluation against seven rigid and three nonrigid methods using a variety of data - simulated, algorithmically generated, and manually annotated - across three vascular anatomies: the hepatic artery, coronary artery, and aorta. Our findings show the proposed method's resistance to pose variations, noise, and deformations, outperforming existing methods in terms of registration accuracy and computational efficiency. The proposed method demonstrates average registration errors of 2.14 mm and 0.34 mm for rigid and nonrigid registration, and an average computation time of 0.51 s.

**Index Terms**—3D/2D registration, vessel graph matching, Monte Carlo tree search, manifold regularization.

## I. INTRODUCTION

DIGITAL subtraction angiography (DSA) is the primary imaging method used in minimally invasive vascular interventions, which uses X-rays to penetrate tissues and translate path information onto a 2D image. In order to observe the artery effectively and clearly, the contrast agent is injected into the vascular lumen of interest through the guiding catheter. Although DSA has a high spatial and temporal resolution, it lacks spatial depth information. In addition, excessive use of toxic contrast agents may increase a patient's physical burden. Therefore, a fusion of the projection of 3D vessels extracted from preoperative computed tomography angiography (CTA) images with DSA is an actual application of 3D/2D registration technology. It provides interventional radiologists with vessel depth information while supporting the manipulation of the guidewire or catheter with low contrast agents.

The challenges of 3D/2D vessel registration are categorized into three major aspects:

- **Rigid Registration Methods:** These methods are largely pose-dependent and sensitive to noise. Many attempts have been made to improve them. Notably, vessel orientation has been used to enhance the optimization process, as seen in [1]. Topological continuity constraints have also been introduced, which has proven effective [2], [3], [4], [5].
- **Vascular Elastic Deformation Models:** The deformation patterns of these models vary widely, and it can be advantageous to establish a generalized model. Some research has been centered on the deformation patterns

of coronary arteries [6], [7], [8]. Other studies have targeted deformation patterns based on statistical shape models [1], [9]. One unique characteristic of vessels is their tree-like topology. By integrating this feature into the deformation models, more realistic deformations can be generated.

- **Intraoperative Real-time Interventional Guidance:**

This is a common application scenario of 3D/2D registration. There is a pressing need to enhance the computational efficiency of elastic registration. The goal is to keep pace with the current DSA video rate of about 10-15 frames per second.

The features utilized in vascular registration methods include: (1) distance measures (Euclidean, Mahalanobis, etc.) between structures (edges, nodes, bifurcations, centrelines, etc.) extracted from the vessels, (2) the direction of the vessels (from the root node to the nodes), and (3) consistency of the topology of the vessels. Indeed, when performing 3D-to-2D perspective projection, the distance measures and directional information undergo dimensionality reduction. However, the vascular topology remains invariant across modalities and dimensions, making it an effective feature for 3D/2D registration. Graph matching, which leverages the consistent topology of vessels, can be utilized as a powerful method for achieving accurate registration in such scenarios [8], [10], [11], [12], [13].

This study aims to propose a vessel 3D/2D registration that can automatically achieve rigid and nonrigid registration with high accuracy. Based on the previous work, the rigid registration is achieved by Monte Carlo Tree Search for 3D/2D registration (MCTS) [4]. In brief, based on vascular topology, we decomposed the vessel matching into continuous correlated states and further constructed as tree structure. Each node of the search tree records the current 3D/2D vessel matching state, as well as the corresponding registration result and evaluation score. The MCTS strategy is applied to detect the optimal matching state with the highest score. For the nonrigid registration, dense correspondences between 3D and 2D vessels are required. Therefore, based on the vessel matching from rigid registration result, we propose a manifold regularization-based vessel deformation model, which forces the deformation field smooth on the vascular topology. It utilizes the inherent topology of vascular structure to construct the manifold regularization term of the objective function. In addition, compared with the complex gradient formulation of the objective function constructed by constraining deformation field smoothing and vessel length variation in 3D/2D vessel registration by Groher et al. [14], we design a simpler gradient formulation, thus prominently improving the efficiency of the nonrigid registration. In conclusion, the main contribution of this work is proposing a fast and accurate method for 3D/2D vascular registration algorithm based on MCTS and manifold regularization, as well as validating the accuracy and efficiency of the algorithm on the clinical hepatic artery, coronary arteries, and aorta datasets. The proposed deformation model only exploits the smoothness of the deformation field in 3D space and the topology; therefore, it can be generalized to arbitrary 3D to 2D cross-dimensional registration of topological data.

The main contributions of this paper are:

- Based on the concept of vessel graph matching, we use MCTS to solve rigid registration and obtain accurate dense matching relations of 3D and 2D vessel point;
- Using the matching relations as input, we propose a generalized vascular deformation model, which has a more free deformation pattern, constrains only the spatial smoothing and topological smoothing of deformation fields, and derives a simple gradient calculation formula, which can quickly achieve nonrigid registration calculation.

The remainder of this paper is organized as follows. Section II reviews related work in the view of transformation and registration principle. Methodological details of our proposed 3D/2D registration method is presented in Section III. The results of our validation and application are shown in Section IV. Lastly, section V provides the discussion and concluding comments.

## II. RELATED WORKS

3D/2D registration typically involves three sequential steps: initialization, rigid registration, and nonrigid registration. While previous research has covered various initialization approaches such as alignment of patient position and orientation, registration of artificial markers, and manual initialization [15]. However, automatic initialization methods [16], [17], [18] with intrinsic features is more suitable for intraoperative 3D/2D registration. Due to the rotational, translational, and projection invariance of vascular topology, we leverage vascular topology matching to achieve automatic pose initialization.

The rigid transformation has received considerable attention in the published 3D/2D registration literature. Nonrigid deformation produced by respiratory and cardiac motion should be compensated for coronary artery and hepatic vessel registration to obtain high accuracy. The difference between rigid and nonrigid registrations is the adopted transformation. Rigid transformation in 3D/2D registration involves three translations and three rotations, while nonrigid transformation is more complex. The vessel deformation model in 3D/2D registration is generally derived from the classical models, such as the statistical shape model (SSM) [19] and thin-plate spline [20]. Groher et al. [14] proposed a vascular deformation model, which penalizes the changes in vascular length and unnatural bending in the energy function. Afterward, Groher et al. [21] formulated the registration problem as an energy minimization problem containing external energy dominated by the response of image information and internal energy dominated by the constraint of 3D vascular length change. Rivest-Henault et al. [22] used the registration energy function constructed by internal and external energies similar to [21]. The difference is that the deformation constraints at vessel bifurcations were introduced into the external energy, and the displacement of 3D centerlines was solved in biplane angiography. Baka et al. [9] extracted the 3D+ $t$  coronary centerlines from the real clinical coronary 4D CTA data and constructed the SSM. Serradell et al. [6] proposed a prior-based approach, leveraging cardiac motion,

to describe vascular deformation using recursive 3D model parameterization. They devised an iterative 3D-to-2D matching framework for calculating the optimal parameters of the model. Wu et al. [7] extended the model by designing a point set-based deep neural network that takes pairs of centerline point sets as input. In this network, the displacements of vessel points were treated as trainable parameters, and classical metrics such as distance error and smoothness were employed as the loss function. The nonrigid deformation model in this work offers increased degrees of freedom, solely imposing constraints on the smoothness of the deformation field in three-dimensional space and vascular topology. We have identified the computational complexity associated with the gradient formulation in [14]. Consequently, we have endeavored to derive a simpler closed-form gradient formulation for the cost function, aiming to expedite the registration process.

According to the registration principles, the 3D/2D registration methods can be classified into two classes, namely, intensity- and feature-based methods. Intensity-based methods are conducted by optimizing the similarity measure between the projection of a 3D pre-interventional image and a 2D intra-interventional image. Digitally reconstructed radiographs (DRR) [23] and maximum intensity projection (MIP) [24] are standard methods that generate simulated X-ray projections of computed tomography (CT) images. Hipwell et al. [25] analyzed six similarity metrics between DRR/MIP and X-ray images, in which pattern intensity and gradient difference exhibited the best performance. Ruijters et al. [26] proposed a 3D/2D registration method that combines intensity information and centerline features. They constructed an objective function using the distance transform of the 3D vessel centerline and the Vesselness response of the DSA image, aiming to reduce reliance on intraoperative image vessel segmentation.

Feature-based 3D/2D registration methods require crossing modal and dimensional features. The vascular centerlines are the most commonly used features in vascular registration methods [15]. The iterative closest point (ICP) method [27] alternately estimates correspondences and transformation, in which the nearest neighbor relation assigns the correspondences, and a closed-form solution typically obtains the transformation. By back-projecting 2D points into 3D space and performing general ICP, an extension of ICP for 3D/2D registration [1] is achieved. To accelerate the ICP process, Rivest-Henault et al. [22] designed an objective function that uses a pre-calculated 2D distance transform of the vascular centerline. Benseghir et al. [28] proposed an iterative closest curve (ICC) method, using the closest relation of the vascular segment curve instead of points to construct the objective function.

The ICC method is an early approach that utilizes the correspondence between branches of vascular centerlines to compute 3D/2D registration. Subsequently, an increasing number of research works have focused on advancing vascular centerline analysis, particularly in terms of vascular centerline topology. Serradell et al. [29] treated vessel registration as a search process for most likely correspondences and conducted a priority search to accelerate the process. Pinheiro et al. [10] formulated vessel matching as a tree search method based on the topology consistency of two graphs, which was

later solved by the Monte Carlo tree search (MCTS). Feuillâtre et al. [12] advanced a method leveraging association graphs and maximum clique for matching a 3D coronary artery tree sequence. Concurrently, Garcia et al. [13] devised an adaptive graph matching technique to manage nonrigid intra-operative deformations up to 65 mm, computing a complete organ displacement field from the matched vasculature. The above methods are related to 3D/3D or 2D/2D vascular matching/registration. For 3D/2D registration of topological vessel structures, Benseghir et al. [2] proposed matching tree centerlines in a divide-and-conquer framework while ensuring the connectivity of bifurcation points.

The vascular topology is also adopted in our previous works. An iterative closest graph matching algorithm was proposed [8], in which the correspondence between 3D and 2D vessels was estimated using a redundant graph matching method, and a closed-form solution of the perspective- $n$ -points (PnP) problem [30] was utilized to estimate the rigid transformation between 3D and 2D points. Furthermore, based on the topological continuity of vessels, the registration and matching of 3D and 2D vessels can be decomposed into continuous states. Thus, the solution space of rigid registration can be degraded by constructing a search tree for the registration problem, which can theoretically improve the effectiveness of solution searching. We tried greedy and heuristic strategy for the search tree problem [5]. To improve the search ability, an improved strategy denoted as MCTS [4], which can balance the exploitation on visited nodes and exploration on unvisited nodes, was proposed.

### III. METHODS

The work flow of vascular 3D/2D registration and its application is shown in Fig. 1(a). Preprocessing, rigid registration, nonrigid registration, and intra-operative fusion are involved. The 3D/2D registration aims to find the optimal spatial transformation that transforms 3D vessels into the target space of DSA acquisition equipment. Then, the 3D vessels can be projected onto a 2D plane according to the imaging parameters of DSA and overlap with the 2D vessels. In this section, we firstly introduced the preprocessing involving vessel segmentation method and vessel graph construction. Then, we introduced the solutions of rigid and nonrigid registration, respectively. The rigid solution has been introduced in our previous work [4], we will briefly describe it in this work.

#### A. Preprocessing

**1) 3D and 2D Vessel Segmentation:** For CTA vessel segmentation, we employed a framework that combines coarse and fine segmentation [31]. This method utilizes  $128 \times 128 \times 64$ -sized image as input for coarse segmentation and cubic patches of size  $16^3$ ,  $32^3$ , and  $64^3$  for fine segmentation. The segmentation results from the different stages and modules are then fused to obtain the final vessel segmentation. We employed a publicly available dataset of 1000 coronary CTA images from 1000 patients [31] to train our 3D coronary artery vessel segmentation model.

For DSA vessel segmentation, we utilized a full resolution UNet with a multiresolution convolution interactive

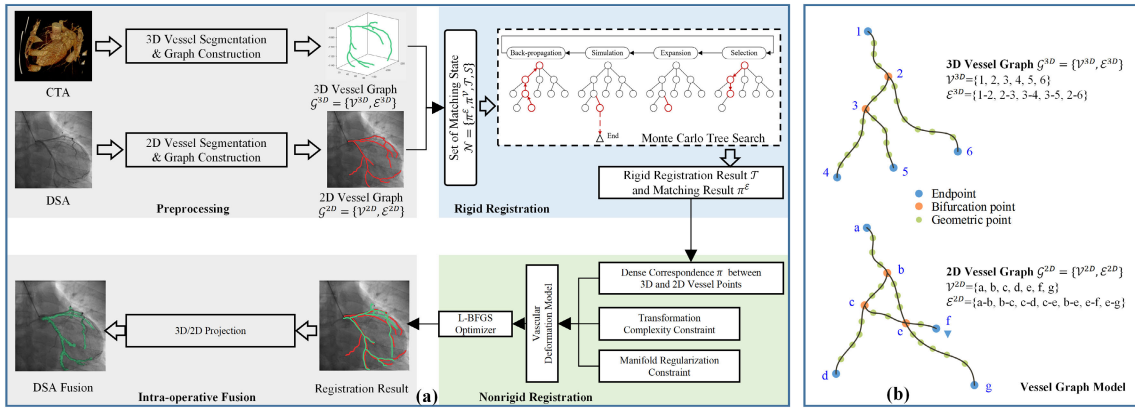


Fig. 1. Work flow of vascular 3D/2D registration and vessel graph model. (a) Workflow involves four sequential steps: preprocessing, rigid registration, nonrigid registration, and intra-operative fusion. (b) Up: 3D vessel graph, Down: 2D vessel graph.

mechanism [32]. This approach involves stacked convolutions at the image resolution to continuously learn full-resolution representations for precise pixel-level segmentation. Our 2D coronary artery segmentation model was trained using two coronary DSA datasets. These include a total of 448 images, with 314 images from 99 patients as reported in [33] and 134 images from another dataset detailed in [34].

**2) 3D and 2D Vessel Graphs:** The 3D/2D registration in this paper relies on accurate vessel graphs obtained from 3D and 2D images, making the construction of vessel graphs crucial. For the segmentation results of 3D and 2D vessels, we first employ a thinning method to obtain the 3D and 2D vessel centerlines. Then, utilizing neighborhood relationships (8)-neighborhood for 2D vessel and 26-neighborhood for 3D vessel), we determine the neighboring points for each point on the centerline, thus obtaining the centerline point sets  $\mathbf{P} \in \mathbb{R}^{N \times D}$  and adjacency matrix  $\mathbf{A} \in \{0, 1\}^{N \times N}$  for each vessel. Subsequently, by analyzing the connectivity of the adjacency matrix  $\mathbf{A}$ , we can identify the endpoints, bifurcation points, geometric point of the vessel centerlines, as depicted in Fig. 1(b), which allows us to construct the vessel graph model  $\mathcal{G} = \{\mathcal{V}, \mathcal{E}\}$ , where  $\mathcal{V}$  denotes the vertex set containing vascular endpoints and bifurcations,  $\mathcal{E}$  denotes the edge set of the vessel branch curve connecting two adjacent vertices.

The 3D vessel graph is typically a strictly acyclic directed graph with a root node where blood flow enters and other endpoints where it exits. For 2D vessel graph, due to projection overlap, there may be overlapping branches that create pseudo-bifurcation points in the 2D view, such as point  $e$  in Fig. 1(b). Some researchers [35], [36] have addressed this issue by utilizing the morphological information of the vessels to identify vessel branches. The resulting branch identification involves disconnecting and reconnecting the vessels at the pseudo-branching points, thereby constructing a cyclic directed 2D vessel map. However, this strategy carries the risk of identification errors, as incorrect disconnections and connections may result in changes to the vessel topology. This poses a significant challenge for registration and matching algorithms that rely on accurate vessel topology information. To address this issue, we introduce the concept of superedges [10], which are defined as sequences of multiple connected edges. By incorporating our proposed MCTS-R

method [4], we can effectively leverage the vessel topology information to achieve registration.

### B. Definition of 3D/2D Vessel Registration

The 3D and 2D vessel graphs are formulated as  $\mathcal{G}^{3D} = \{\mathcal{V}^{3D}, \mathcal{E}^{3D}\}$  and  $\mathcal{G}^{2D} = \{\mathcal{V}^{2D}, \mathcal{E}^{2D}\}$ . Registration of the 3D and 2D vessel structure can be formulated as finding an optimal transformation  $\mathcal{T}$  of the 3D vessel, whose projection can best align the 2D vessel. We have:

$$\mathcal{T}^* = \arg \min_{\mathcal{T} \in \Omega_{\mathcal{T}}} \mathcal{D}(\mathcal{P} \circ \mathcal{T}(\mathcal{G}^{3D}), \mathcal{G}^{2D}), \quad (1)$$

where  $\mathcal{D}$  quantifies the distance between two registered vessel graphs.  $\mathcal{P}$  denotes a constant and mandatory perspective projection operation to register 3D and 2D modalities. This can be established using several parameters obtained from the DICOM head file of XRA [37].

$\mathcal{T}$  denotes 3D rigid or nonrigid transformation and  $\Omega_{\mathcal{T}}$  is the domain of admissible transformation. For rigid registration,  $\mathcal{T}$  includes three translations and three rotations.  $\Omega_{\mathcal{T}}$  can be formulated as special Euclidean group  $SE(3)$ ,

$$\Omega_{\mathcal{T}} = SE(3) = \left\{ \begin{bmatrix} \mathbf{R} & \mathbf{t} \\ \mathbf{0} & 1 \end{bmatrix} \mid \mathbf{R} \in SO(3), \mathbf{t} \in \mathbb{R}^{3 \times 1} \right\}$$

$$SO(3) = \{ \mathbf{R} \in \mathbb{R}^{3 \times 3} \mid \mathbf{R}^T = \mathbf{I}, \det(\mathbf{R}) = 1 \}. \quad (2)$$

where  $SO(3)$  denotes special orthogonal group. In this work, we build a set of matching states for 3D and 2D vessel graphs, then the solution space of rigid registration can be simplified to a limited search tree space. Compared with solution searching based on gradient descent, that based on tree structure has advantages on efficiency and global searching ability.

For nonrigid registration, The degree of freedom of deformation model is determined by the dimension of model parameters. Thus,  $\mathcal{T}$  is generally represented as a multidimensional space, and the Tikhonov regularization [38] is used to punish the complexity of deformation model and solve it.

### C. Monte Carlo Tree Search for Rigid Registration

Two surjections  $f_1 : \pi \in \Omega_{\pi} \rightarrow \mathcal{T} \in \Omega_{\mathcal{T}}$  and  $f_2 : \pi^{\mathcal{E}} \in \Omega_{\pi^{\mathcal{E}}} \rightarrow \pi \in \Omega_{\pi}$  are introduced [4], where  $\Omega_{\pi}$  is the domain of matching between 3D and 2D vessel points  $\pi$ ,  $\Omega_{\pi^{\mathcal{E}}}$  denotes the domain of matching between 3D and 2D edges  $\pi^{\mathcal{E}}$ .

Based on the  $\pi^{\mathcal{E}}$  definition and topological continuity, we can gradually pair edges along with the vascular graph when the initial matched vertex pair is given,  $\pi_{t+1}^{\mathcal{E}} = \pi_t^{\mathcal{E}} \cap (e_i^{3D}, e_j^{2D})$ . According to the contiguous states of edge matching, a search tree  $\Omega_{\pi^{\mathcal{E}}}$  can be constructed. The optimal  $\pi^{\mathcal{E}}$  can be obtained by searching the tree space  $\Omega_{\pi^{\mathcal{E}}}$ . Here, an evaluation score associated with registration is designed. Then, we have:

$$Q = \frac{1}{|\mathbf{P}^{3D}|} \sum_i e^{-\left(\min_j ||\mathcal{P} \circ \mathcal{T}(p_i^{3D}) - p_j^{2D}||\right)/\sigma} + e^{-\left(\frac{s^{3D}}{s^{2D}} + \frac{s^{2D}}{s^{3D}} - 2\right)}, \quad (3)$$

where  $p_i^{3D}$  and  $p_j^{2D}$  denote the 3D and 2D points, respectively.  $\mathbf{P}^{3D}$  denotes the counts of 3D points. For a given  $\pi^{\mathcal{E}}$ , the transformation can be estimated through the two surjections  $\mathcal{T} = f_1(f_2(\pi^{\mathcal{E}}))$ . The first item of the score is associated with the overlapping degree. The minimal distance between the projected 3D point  $\mathcal{P} \circ \mathcal{T}(p_i^{3D})$  and 2D point  $p_j^{2D}$  can be computed using distance transform, and  $\sigma$  is the scale parameter to normalize the distance. The second item is employed to penalize the scaling in 3D-to-2D projection.  $s^{2D}$  and  $s^{3D}$  denote the distribution scales of projected 3D vertex points  $\mathcal{V}^{3D}$  and 2D vertex points  $\mathcal{V}^{2D}$ , respectively. The distribution scale of the point set can be calculated using a variant of the generalized variance [39],  $s = \det(\Sigma)^{1/2d}$ , where  $\Sigma$  is the covariance matrix of point set,  $d$  denotes the dimension, and the power term is used to normalize the 3D and 2D scales.

The score defined in Eq. 3 is used as the reward of each node. The key step for the highest MCTS is to find a node with the highest reward in the domain  $\Omega_{\pi^{\mathcal{E}}}$  and to accurately select the child nodes of the current state. This goal can be achieved by iteratively constructing a partial search. MCTS extends a partial search tree iteratively using four steps, selection, expansion, simulation, and back-propagation. These four steps are iterated until a computational budget is reached or the theoretical maximum reward is obtained. The node with the maximum reward value is obtained from the built partial search tree after the iteration, and the final results of this method are the corresponding  $\pi^{\mathcal{E}}$  and rigid transformation  $\mathcal{T}$ .

#### D. Manifold Regularized Deformation Model for Nonrigid Registration

Given the correspondences of 3D and 2D points,  $\pi = \{(p_i^{3D}, p_j^{2D})\}$ , let  $\mathbf{Y} = [\mathbf{y}_1, \mathbf{y}_2, \dots, \mathbf{y}_K] \in \mathbb{R}^{K \times 3}$  and,  $\mathbf{X} = [\mathbf{x}_1, \mathbf{x}_2, \dots, \mathbf{x}_K] \in \mathbb{R}^{K \times 2}$ , represent the 3D and 2D points matrix, respectively, where  $\mathbf{y} \in \mathbb{R}^{3 \times 1}$  and  $\mathbf{x} \in \mathbb{R}^{2 \times 1}$  are the coordinates of 3D and 2D points, respectively. The corresponding points in both sets have the same index,  $K$  is the counts of the point set. The purpose of nonrigid registration is to estimate the spatial transformation  $\mathcal{T}$  which makes  $\mathcal{P} \circ \mathcal{T}(\mathbf{y}_k) = \mathbf{x}_k$ . The transformation of a 3D point is expressed as  $\mathcal{T}(\mathbf{y}_k) = \mathbf{y}_k + \delta(\mathbf{y}_k)$ , where  $\delta(\cdot)$  is the displacement function. The 3D/2D nonrigid registration is ill-posed, thus the regularization operated in Reproducing Kernel Hilbert Space (RKHS) [40] is employed. Let  $\mathcal{H}$  be an RKHS, and we use the Tikhonov regularization [38] to minimize the following cost

function to obtain a spatial transformation  $\mathcal{T}$  defined in  $\mathcal{H}$ . We have:

$$\mathcal{T}^* = \arg \min_{\mathcal{T} \in \mathcal{H}} \left\{ \frac{1}{K} \sum_{k=1}^K \|\mathbf{x}_k - \mathcal{P} \circ \mathcal{T}(\mathbf{y}_k)\|^2 + \lambda \|\mathcal{T}\|_{\mathcal{H}}^2 \right\}. \quad (4)$$

The first item penalizes the projected displacement between 3D and 2D vessels, and the second item penalizes the excessive deformation fields of 3D vessel,  $\lambda$  is the coefficient to balance the two items, and  $\|\cdot\|_{\mathcal{H}}$  is the RKHS norm. For the transformation,  $\mathcal{T}$  defined in RKHS can be expressed as a linear combination of arbitrary reproducing kernel functions, we have:

$$\mathcal{H} := \left\{ \mathcal{T} \mid \mathcal{T} = \sum_{i=1}^N w_i k(c_i, \cdot), w_i \in \mathbb{R}, c_i \in \mathcal{C}, N \in \mathbb{N} \right\} \quad (5)$$

where  $k$  is a positive definite kernel function,  $k : \mathcal{C} \times \mathcal{C} \mapsto \mathbb{R}$ ,  $\mathcal{C}$  is an arbitrary non-empty set.  $c_i \in \mathcal{C}$  is the input of the kernel function. Thus, the RKHS norm can be calculated using an inner product  $\|\cdot\|_{\mathcal{H}} = \sqrt{\langle \cdot, \cdot \rangle_k}$ . In this study, the Gaussian function  $\phi$  is adopted as the kernel function. Then the spatial transformation can be calculated as follows:

$$\mathcal{T}(\mathbf{y}_k) = \sum_{i=1}^C \mathbf{w}_i \phi(\mathbf{c}_i, \mathbf{y}_k) \quad (6)$$

where  $\mathbf{c}_i \in \mathbb{R}^{3 \times 1}$  is the input of Gaussian function  $\phi$ ,  $\mathbf{C} = [\mathbf{c}_1, \mathbf{c}_2, \dots, \mathbf{c}_C]^T \in \mathbb{R}^{C \times 3}$  is the matrix of input control points,  $C$  is the counts of control points. The kernel function is formulated as  $\phi(\mathbf{c}_i, \mathbf{y}_k) = \exp(-\|\mathbf{c}_i - \mathbf{y}_k\|/\beta^2/2)$ ,  $\beta$  is the kernel size,  $\mathbf{w}_i \in \mathbb{R}^{3 \times 1}$  is the coefficient of transformation  $\mathcal{T}$ . Equation (6) can be written as a matrix form  $\mathcal{T}(\mathbf{y}_k) = \mathbf{W}^T \Phi(\cdot, k)$ ,  $\mathbf{W} = [\mathbf{w}_1, \mathbf{w}_2, \dots, \mathbf{w}_C]^T \in \mathbb{R}^{C \times 3}$  is the coefficient matrix,  $\Phi(\cdot, k)$  is the  $k$ -th column of matrix  $\Phi \in \mathbb{R}^{C \times K}$ , the entries of  $\Phi$  are  $\phi_{i,k} = \phi(\mathbf{c}_i, \mathbf{y}_k)$ . In addition, the transformation of the 3D point set  $\mathbf{Y}$  can be written as  $\mathcal{T}(\mathbf{Y}) = [\mathcal{T}(\mathbf{y}_1), \mathcal{T}(\mathbf{y}_2), \dots, \mathcal{T}(\mathbf{y}_K)]^T$ . Thus,  $\mathcal{T}(\mathbf{Y}) = \mathbf{T} = \Phi^T \mathbf{W}$ . According to the RKHS definition, the norm of  $\mathcal{T}$  can be calculated using its inner product,

$$\begin{aligned} \|\mathcal{T}\|_{\mathcal{H}}^2 &= \langle \mathcal{T}(\cdot), \mathcal{T}(\cdot) \rangle_k \\ &= \left\langle \sum_{i=1}^C \mathbf{w}_i \phi(\mathbf{c}_i, \cdot), \sum_{j=1}^C \mathbf{w}_j \phi(\mathbf{c}_j, \cdot) \right\rangle \\ &= \sum_{i=1}^C \sum_{j=1}^C \mathbf{w}_i^T \mathbf{w}_j \langle \phi(\mathbf{c}_i, \cdot), \phi(\mathbf{c}_j, \cdot) \rangle \\ &= \sum_{i=1}^C \sum_{j=1}^C \mathbf{w}_i^T \mathbf{w}_j \phi(\mathbf{c}_i, \mathbf{c}_j) \\ &= \text{tr}(\mathbf{W}^T \mathbf{U} \mathbf{W}) \end{aligned} \quad (7)$$

where the entries of the matrix,  $\mathbf{U} \in \mathbb{R}^{C \times C}$ , are  $u_{i,j} = \phi(\mathbf{c}_i, \mathbf{c}_j)$ , and  $\text{tr}(\cdot)$  denotes the matrix trace.

The norm of transformation  $\|\mathcal{T}\|_{\mathcal{H}}^2$  restrains the smoothness of the deformation field described by the control points  $\mathbf{C}$  and coefficient matrix  $\mathbf{W}$ . For 3D/2D registration, the displacement restraint of 3D points on the vessel topology is adopted. Let

$\mathbf{A} \in \{0, 1\}^{K \times K}$  denote the adjacent matrix of 3D points, if  $y_i$  and  $y_j$  are connected,  $a_{i,j} = 1$ , otherwise  $a_{i,j} = 0$ . Therefore, we propose a norm  $\|\mathcal{T}\|_{\mathcal{M}}^2$  in the manifold  $\mathcal{M}$  of vessel points to further restrain the smoothness of deformation on vessels topology. Described as the consistency of the displacements of adjacent points on the topology, we have:

$$\|\mathcal{T}\|_{\mathcal{M}}^2 = \sum_{i=1}^K \sum_{j=1}^K a_{i,j} (\delta(y_i) - \delta(y_j))^2. \quad (8)$$

It is evident that the manifold norm also restrains the change of vessel length, which is popularly used in related works [14], [21]. According to the definition of graph Laplacian,  $\|\mathcal{T}\|_{\mathcal{M}}^2$  can be formulated as manifold regularization. Let  $\mathbf{D}$  denotes the degree matrix of  $\mathbf{A}$ ,  $\mathbf{D} = \text{diag}(\sum_{j=1}^K a_{i,j})_{i=1}^K$ , the Laplacian matrix  $\mathbf{L} = \mathbf{D} - \mathbf{A}$ . Let  $\Delta = [\delta(y_1), \delta(y_2), \dots, \delta(y_K)] \in \mathbb{R}^{K \times 3}$  denotes the displacement matrix of 3D points, then (8) can be written as  $\|\mathcal{T}\|_{\mathcal{M}}^2 = \text{tr}(\Delta^T \mathbf{L} \Delta)$ . Thus, the cost function of nonrigid 3D/2D vessel registration can be formulated as follows:

$$\begin{aligned} Q(\mathbf{W}) = \frac{1}{K} \sum_{k=1}^K & \|x_k - \mathcal{P}(\mathbf{W}^T \Phi(\cdot, k))\|^2 \\ & + \lambda_1 \text{tr}(\mathbf{W}^T \mathbf{U} \mathbf{W}) + \lambda_2 \text{tr}(\Delta^T \mathbf{L} \Delta), \end{aligned} \quad (9)$$

where  $\mathbf{W}$  is the deformation parameter,  $\lambda_1$  and  $\lambda_2$  are weight coefficients.

The L-BFGS algorithm [41] is applied to optimize the cost function; thus  $\partial Q / \partial \mathbf{W}$  is required. The derivative of the first item  $Q_1$  is calculated first. Let  $\mathbf{t}_k = \mathcal{T}(y_k)$ ,  $Q_1 = \frac{1}{K} \sum_{k=1}^K \|x_k - \mathcal{P}(\mathbf{t}_k)\|^2$ . Since  $\mathbf{T} = \Phi^T \mathbf{W}$ , we have:

$$\frac{\partial Q_1}{\partial \mathbf{W}} = \frac{\partial \mathbf{T}}{\partial \mathbf{W}} \frac{\partial Q_1}{\partial \mathbf{T}} = \Phi \frac{\partial Q_1}{\partial \mathbf{T}}. \quad (10)$$

For  $\frac{\partial Q_1}{\partial \mathbf{T}} = [\partial Q_1 / \partial \mathbf{t}_1, \partial Q_1 / \partial \mathbf{t}_2, \dots, \partial Q_1 / \partial \mathbf{t}_K]^T \in \mathbb{R}^{K \times 3}$ , we calculate each  $\partial Q_1 / \partial \mathbf{t}_k$  as follow,

$$\frac{\partial Q_1}{\partial \mathbf{t}_k} = -\frac{2}{K} (x_k - \mathcal{P}(\mathbf{t}_k))^T \mathbf{J}_k, \quad (11)$$

where  $\mathbf{J}_k \in \mathbb{R}^{2 \times 3}$  is the Jacobian of  $\mathcal{P}$  with respective to  $\mathbf{t}_k$ ,

$$\begin{aligned} \mathbf{J}_k = \frac{1}{(\mathbf{p}_3^T \hat{\mathbf{t}}_k)^2} & \begin{bmatrix} p_{11} \mathbf{p}_3^T \hat{\mathbf{t}}_k - p_{31} \mathbf{p}_1^T \hat{\mathbf{t}}_k & p_{21} \mathbf{p}_3^T \hat{\mathbf{t}}_k - p_{31} \mathbf{p}_2^T \hat{\mathbf{t}}_k \\ p_{12} \mathbf{p}_3^T \hat{\mathbf{t}}_k - p_{32} \mathbf{p}_1^T \hat{\mathbf{t}}_k & p_{22} \mathbf{p}_3^T \hat{\mathbf{t}}_k - p_{32} \mathbf{p}_2^T \hat{\mathbf{t}}_k \\ p_{13} \mathbf{p}_3^T \hat{\mathbf{t}}_k - p_{33} \mathbf{p}_1^T \hat{\mathbf{t}}_k & p_{23} \mathbf{p}_3^T \hat{\mathbf{t}}_k - p_{33} \mathbf{p}_2^T \hat{\mathbf{t}}_k \end{bmatrix}^T, \end{aligned} \quad (12)$$

where  $p_{ij}$  denotes the entries of projection matrix  $\mathbf{P} \in \mathbb{R}^{3 \times 4}$ ,  $\mathbf{p}_1^T$ ,  $\mathbf{p}_2^T$  and  $\mathbf{p}_3^T$  are the row vectors of  $\mathbf{P}$ ,  $\hat{\mathbf{t}}_k$  is the homogeneous form of  $\mathbf{t}_k$ . Detailed deduction of  $\mathbf{J}_k$  refers to [14]. The derivative of the second item  $Q_2 = \lambda_1 \text{tr}(\mathbf{W}^T \mathbf{U} \mathbf{W})$  can be calculated as follows:

$$\frac{\partial Q_2}{\partial \mathbf{W}} = \lambda_1 (\mathbf{U} + \mathbf{U}^T) \mathbf{W} = 2\lambda_1 \mathbf{U} \mathbf{W}. \quad (13)$$

For the third item  $Q_3 = \lambda_2 \text{tr}(\Delta^T \mathbf{L} \Delta)$ ,  $\Delta = \Phi^T \mathbf{W} - \mathbf{Y}$ , the derivative is calculated as follows:

$$\frac{\partial Q_3}{\partial \mathbf{W}} = \frac{\partial \Delta}{\partial \mathbf{W}} \frac{\partial Q_3}{\partial \Delta} = \lambda_2 \Phi (\mathbf{L} + \mathbf{L}^T) \Delta = 2\lambda_2 \Phi \mathbf{L} \Delta. \quad (14)$$

TABLE I  
INFORMATION OF THE IN-HOUSE VASCULAR DATA USED IN THIS WORK

Anatomy	Hepatic Artery	Aorta	Coronary Arteries
Source	Zhongda Hospital Southeast University	Zhuhai	People's Hospital
Number of Cases	5	12	30
CTA	Image size of slice	512 × 512	
	Resolution of slice	0.793 mm × 0.793 mm	0.35 mm × 0.35 mm
	Thickness	1.25mm	0.625mm
DSA	Image size of DSA	1024 × 1024	512 × 512
	Resolution of DSA	0.2537 mm × 0.2537 mm	0.37 mm × 0.37 mm
Pairs of 3D and 2D Vessels	20	108	34

Based on the above calculations, the derivative  $\partial Q / \partial \mathbf{W}$  of the cost function  $Q$  with respect to the deformation parameters  $\mathbf{W}$  can be obtained.

## IV. EXPERIMENTS AND RESULTS

### A. Experimental Setting

This study performs experiments on the clinical hepatic arteries, coronary arteries, and aorta data. Detailed information on the in-house vascular dataset for 3D/2D registration is presented in Table I, including data sources, image size and image resolution. These datasets are collected from three hospitals, involving intra-patient CTA and DSA. Furthermore, we use public available CTA and DSA datasets for training our deep learning based segmentation models, as described in section III-A. In order to quantitatively assess the robustness of our method and compare it with other approaches regarding pose, deformation, and noise, we employed the vessel simulation data [5], [8].

The projected distance (PD) between projected 3D and 2D centerline points and 3D mean target registration error (TRE) [42] were adopted to evaluate the result of 3D/2D registration. The rigid registration performance of the proposed method is compared with six competing methods: 1) the extension of ICP (ICP-BP) to the 3D/2D application [27]; 2) the accelerated method for ICP matching (DT) by using a precomputed distance transform of 2D vessel centerlines [22]; 3) the tree topology matching for 3D/2D registration (Tree) using tree topology consistency [2]; 4) oriented Gaussian mixture model (OGMM) [1]; 5) greedy tree search for 3D/2D registration (GTSR) [5], 6) heuristic tree search for 3D/2D registration (HTSR) [5], and 7) iterative closest graph matching for non-rigid 3D/2D coronary arteries registration (ICGM) [8]. The nonrigid performance is compared with three competing methods: 1) deformable 3D/2D registration method (Deformable), which penalizes the length change and bending [14]; 2) a synthetic prior vessel deformation model (Prior), applied to 3D/2D vessel registration [6], [8]; 3) a deep learning-based deformation model for 3D/2D coronary artery registration [7] (CAR-Net).

The parameters of our method are selected empirically. We set the node score parameter  $\sigma = 5$ ,  $\gamma = 0.001$ ,  $N_{exp} = 2$ ,  $N_{sim} = 10$ ,  $Q_{max} = 1.8$ ,  $N_{max} = 200$ ,  $\beta = 5$ . The control

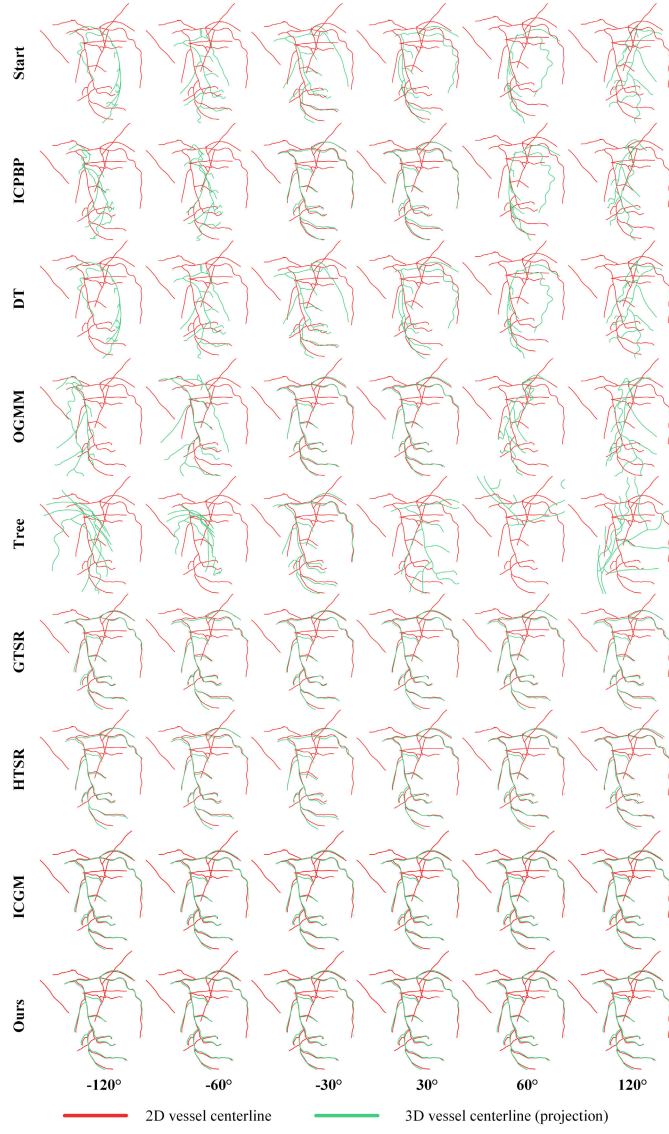


**Fig. 2.** Result demonstration of 3D/2D rigid registration experiment on simulation data of the proposed method and comparative methods. Projected 3D and 2D centerlines are shown in green and red, respectively.

points  $C$  of the deformation model are set randomly in the spatial ranges of 3D vessel points, the counts of control points  $C = 30$ . The weight coefficient  $\lambda_1 = 1$ , and  $\lambda_2 = 0.2/|\mathcal{P}^{3D}|$ .

### B. Experiments on Simulated Data With Defects

In this work, we utilized the simulated data from our previous work [5], [8], which contains a set of dynamic thoracic volume data containing cardiac motion, and includes enhanced structures of the complete heart, coronary arteries, and aorta. The volume data comprised 300 slices with a slice thickness of 0.5mm. The size of each slice image was 400 × 400 pixels, with a pixel spacing of 0.5 mm × 0.5 mm. The volume data was processed using a medical image analysis software (Materialise Mimics) to extract the vessel centerlines and their connectivity, resulting in the construction of a 3D vessel graph  $\mathcal{G}_{sim}^{3D}$ . The simulated 2D vessels can be expressed as  $\mathcal{G}_{sim}^{2D} = \mathcal{P} \circ \mathcal{T}(\mathcal{G}_{sim}^{3D}, b) + \mathcal{N}(\beta)$ , where  $\beta$  represents the proportion of noise added to the simulated data and  $b$  represents the scale of elastic deformation. Furthermore,

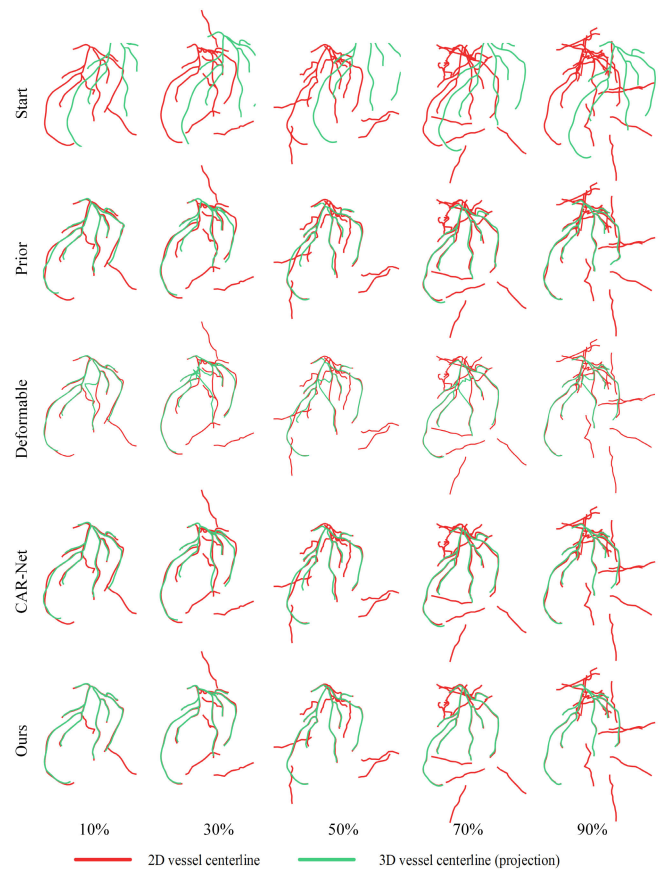


**Fig. 3.** Result demonstration of 3D/2D nonrigid registration experiment on simulation data with noise and deformation. Projected 3D and 2D centerlines are shown in green and red, respectively.

rotated 3D vessels are produced  $\mathcal{G}_{start}^{3D} = \mathcal{T}(\mathcal{G}_{sim}^{3D}, \theta)$  as the start point of registration, where  $\theta$  represents the angle of rotation, as shown in the first row of Fig. 2 and Fig. 3. We used mTRE to evaluate the performance of competing methods, which can be calculated using the mean Euclidean distance of corresponding 3D points  $TRE(\mathcal{T}^*(\mathcal{G}_{start}^{3D}), \mathcal{G}_{sim}^{3D})$ , where  $\mathcal{T}^* = \arg \min \mathcal{D}(\mathcal{P} \circ \mathcal{T}(\mathcal{G}_{start}^{3D}), \mathcal{G}_{sim}^{2D})$ .

The rigid registration experiments were conducted using 48 pairs of randomly generated simulated data with added noise ( $\beta = 50\%$ ) and varying rotation angles, and the rotation angles used encompassed arbitrary rotations around the axis of  $-120^\circ$ ,  $-60^\circ$ ,  $-30^\circ$ ,  $30^\circ$ ,  $60^\circ$ , and  $120^\circ$ . We selected one set of results to showcase in Fig. 2, which includes 6 pairs of vessels and the registration results of 8 methods. The rotation angles are depicted from left to right, and the comparative methods are presented from top to bottom. The detailed results of the mean TRE for 3D/2D rigid registration methods, categorized by different rotation angles, are presented in Table II.

The nonrigid registration experiments were performed using simulated data with deformation ( $b = 1.0$ , rotation angle ( $\theta = 5.0^\circ$ ), and varying levels of noise from 10% to 90%. The noise level is expressed as a corresponding proportion of noise points added based on the current data's point count. The noise primarily consists of small branches and pseudo-vascular structures in simulated DSA images. Therefore, the added noise alters the topology of the 2D vasculature, posing a certain level of challenge for topology-based vascular

TABLE II

MEAN TRE (UNIT: mm) OF 3D/2D RIGID VESSEL REGISTRATION  
ON SIMULATION DATA WITH NOISE ( $\beta = 50\%$ )  
AND VARYING ROTATION ANGLES

	Rotation angle ( $\theta$ )					
	-120°	-60°	-30°	30°	60°	120°
ICP-BP [27]	2.824	3.043	1.188	1.239	3.252	3.351
DT [22]	5.155	4.300	1.921	1.888	3.751	3.759
Tree [2]	7.602	2.937	1.143	1.143	2.163	2.272
OGMM [1]	5.682	2.054	<b>1.136</b>	1.548	3.210	5.500
GTSR [5]	1.212	1.434	1.180	1.180	1.330	1.435
HTSR [5]	1.340	1.434	1.154	1.192	1.200	1.258
ICGM [8]	<b>1.207</b>	1.177	1.202	<b>1.134</b>	1.214	1.161
Ours	1.217	<b>1.139</b>	1.150	1.184	<b>1.198</b>	<b>1.141</b>

TABLE III

MEAN TRE (UNIT: mm) OF 3D/2D NONRIGID VESSEL REGISTRATION  
ON SIMULATION DATA WITH DEFORMATION ( $b = 1.0$ ), ROTATION  
ANGLE ( $\theta = 5.0^\circ$ ), AND VARYING NOISES

	Noise percentage ( $\theta$ )				
	10%	30%	50%	70%	90%
Prior [6]	1.700	1.609	1.678	1.635	1.690
Deformable [14]	2.760	2.720	2.745	3.810	3.767
CAR-Net [7]	1.410	1.299	1.371	1.397	1.395
Ours	<b>0.428</b>	<b>0.391</b>	<b>0.585</b>	<b>0.784</b>	<b>0.393</b>

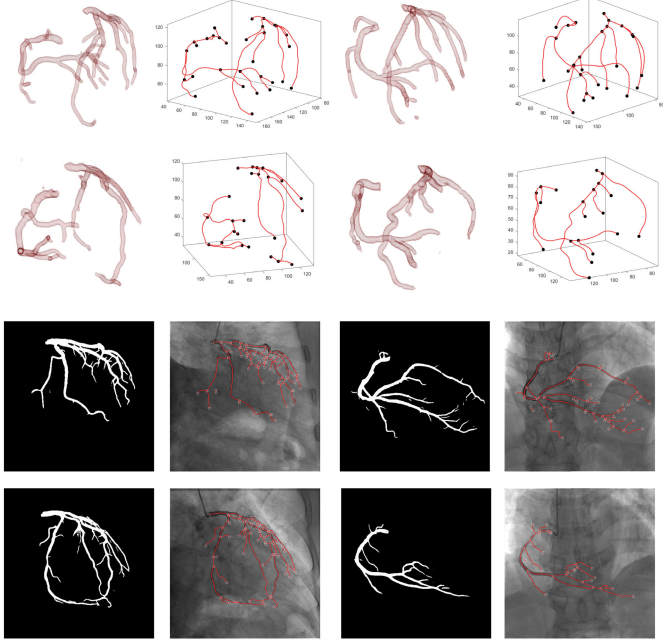


Fig. 4. Showcases of algorithmically generated 3D and 2D coronary artery segmentation masks and vessel graphs.

registration algorithms. Fig. 3 presents the performance of the comparative methods and our proposed method under different noise percentage. The detailed mTRE results are displayed in Table III.

### C. Experiments on Generated Coronary Centerlines

We utilized the segmentation method described in section III-A to segment and compute vessel graphs for coronary CTA and DSA data, resulting in 24 pairs of coronary 3D and 2D vessel graphs with computation-induced defects. We present a subset of these examples in Fig. 4. Upon examining the 3D vessel segmentation results, we observed that the main defects in the segmentation are the under-segmentation of small vessel branches, but overall, the segmentation results

TABLE IV

MEAN PD (UNIT: mm) AND COMPUTATION TIME OF 3D/2D VESSEL  
REGISTRATION ON GENERATED DATA

Methods	PD (mm)	time (s)
Rigid Registration	ICP-BP [27]	3.41
	DT [22]	3.34
	Tree [2]	12.01
	OGMM [1]	2.49
	GTSR [5]	3.16
	HTSR [5]	3.17
Nonrigid Registration	ICGM [8]	2.41
	Ours	<b>2.14</b>
	Prior [6]	2.04
	Deformable [14]	1.39
	CAR-Net [7]	1.24
	Ours	<b>0.34</b>

are still relatively close to manual annotations. Regarding the 2D vessels, due to the inclusion of numerous small vessels in our training dataset, the segmentation results are rich and detailed. We extracted the two largest connected component for the 3D vessels to remove any disconnected parts, while we kept the 2D vessels in their original form without any further processing, aiming to test the robustness of our proposed method and comparative methods against the errors introduced during the preprocessing steps.

Hence, when facing algorithmically generated vascular data, the primary disturbances to registration methods are branch noise and deformations. Unlike simulation data, 3D and 2D vascular data from CTA and DSA devices lack a 3D gold standard. Therefore, we employ the PD to evaluate registration errors and record the computational time, as indicated in Table IV. Unlike the comparative tests in our previous works [4], [5], [8], parts of the codes in this paper were updated, as well as the testing environment and platform, using python and C++ on a high-performance PC with Intel i9 CPU.

Examples of the results for rigid and nonrigid registration are shown in Fig. 5 and Fig. 6, respectively. Fig. 5 displays the registration results for two cases, with the left coronary artery (LCA) shown in the first and second rows, and the right coronary artery (RCA) shown in the third and fourth rows. Fig. 6 showcases the registration results for one LCA case and two RCA cases. The registration methods are indicated below each subfigure.

### D. Experiments on Manually Annotated Vessels

The purpose of conducting registration experiments on manually annotated 3D and 2D vascular data is to eliminate excessive noise and mitigate the interference caused by defects. This allows us to solely consider the impact of different 3D and 2D imaging modalities and structural deformations on registration algorithms. Additionally, it can provide valuable guidance for the design of pre-processing algorithms for vascular registration. The manually annotated data consists of three distinct vascular anatomies: hepatic artery, coronary artery, and aorta. In Fig. 7, we present the vessel graphs obtained through manual annotation of vascular masks. The upper portion depicts the 3D vascular map, while the lower portion showcases the 2D vascular map.

The results of our method are presented in the form of 3D centerlines overlapping the DSA images with 2D centerlines (Fig. 8). The first row indicates the initial state of 3D and 2D

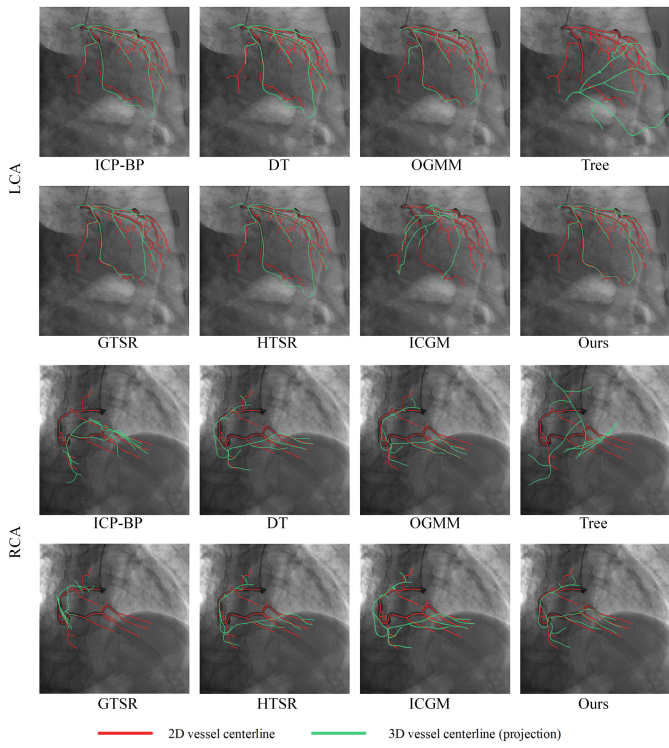


**Fig. 5.** Result demonstration of 3D/2D rigid registration experiment on algorithmically generated LCA and RCA data. Projected 3D and 2D centerlines are shown in green and red, respectively.

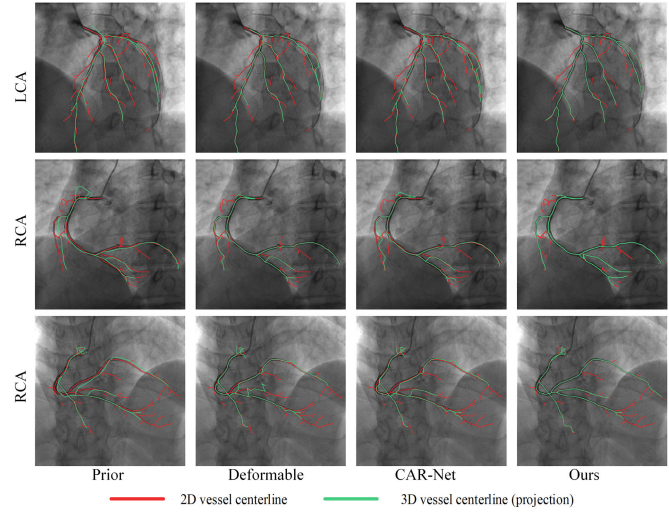


**Fig. 6.** Result demonstration of 3D/2D nonrigid registration experiment on algorithmically generated LCA and RCA data. Projected 3D and 2D centerlines are shown in green and red, respectively.

vessels, while the second row indicates the rigid registration results. Finally, the third row indicates the results of nonrigid registration. Before rigid registration, the 3D and 2D data are automatically aligned to remove the translation difference, whereas the rotations are retained. For nonrigid registrations, same initial rigid transformations are given for all comparison methods. We use the accumulation histogram of error to show the results of all rigid and nonrigid registration algorithms on manually annotated vessels, as shown in Fig. 9. The x-axis of the histogram indicates the PD value in millimeters and the y-axis indicates the percentage. The points on the histogram

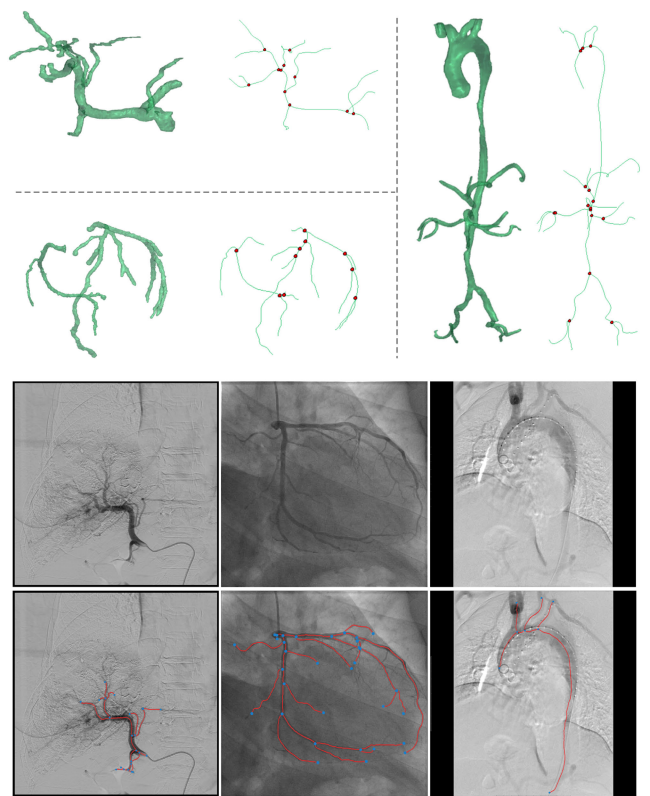


**Fig. 7.** Illustration of 3D and 2D vessel graphs of manually-annotated hepatic artery, coronary artery, aorta.

curve can be expressed as the percentage of cases below this error to all cases.

#### E. Vessel Graph Construction and Matching

The advantages that topology brings to 3D/2D vascular registration include reduced dependence of the algorithm on the initial poses and the generation of more accurate vascular dense matching results, which are also critical to the formation of high-quality deformation models. However, errors in the generated vessel topology also have a large impact on the registration algorithm, and to some extent, the vessel topology-based registration algorithm should first focus on how to generate a high-quality vessel topology or graph. Apart from the effect of CTA vessel segmentation algorithms, 3D vessel graphs can usually be considered accurate. The biggest effect on the structure of the 3D vessel graphs is the inability of the low-resolution CTA to distinguish some adherent vessel walls, resulting in a misaligned vessel topology. This phenomenon may be more common for hepatic arteries; for aorta and coronary arteries, the 3D vessel topography is usually clear. In addition, the 3D vessel graph is acyclic and directed, and the inlet identification of the vessels is also critical, as only the endpoint with the largest radius is determined to be the root node of the vessel tree. We illustrate examples of 3D vessel graphs in Fig. 10. Based on the vessel segmentation, the centerline and the connection relationship between points can be obtained using the skeleton extraction method, then  $\mathcal{G}^{3D} = \{\mathcal{V}^{3D}, \mathcal{E}^{3D}\}$  can be constructed.

The construction of 2D vessel graphs is relatively complicated. Due to the principle of DSA fluoroscopic imaging,

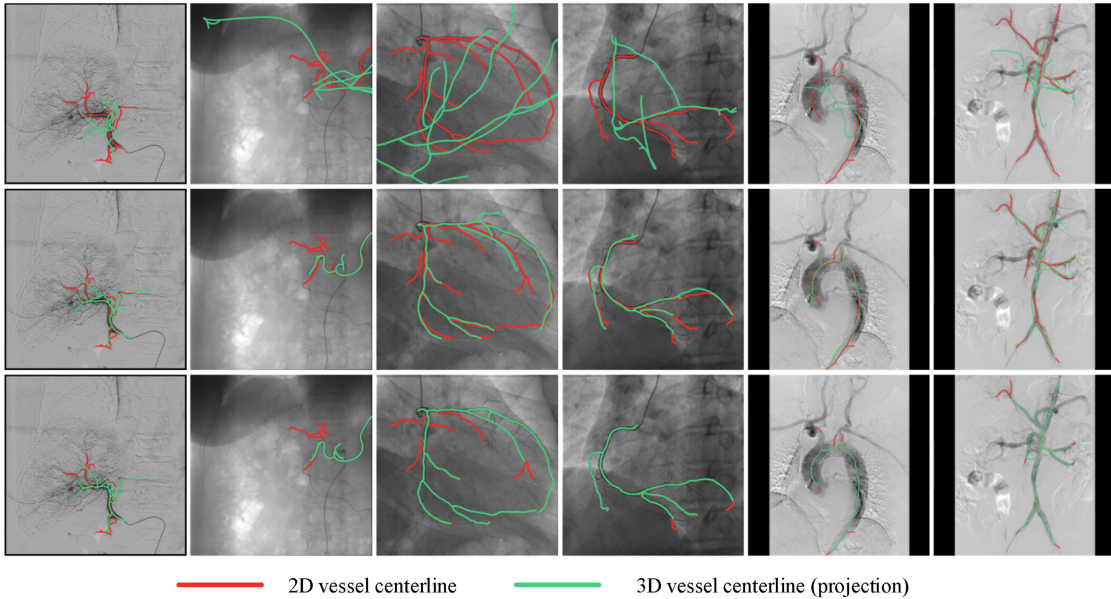


**Fig. 8.** Result demonstration of vessel 3D/2D registration. The columns from left to right indicate hepatic artery, coronary artery, and aorta, respectively. The rows from up to down indicate initial states, rigid registration results, and nonrigid registration results, respectively. The mean project distance is displayed below corresponding case.

2D vessel branches may overlap in plane, and there is no such method that can accurately reconstruct vessel topology in DSA fluoroscopic images. In clinical practice, the interventionalist usually choose a better C-arm angle to obtain a better unfolding of the vessel in the plane in order to distinguish different branches, as shown in Fig. 8. The 2D vessel graphs we constructed will not identify overlap and pseudo-branching, i.e., the 2D vessel graphs may be looped. Based on 2D vessel segmentation, we first thinning the segmentation result, and then adopt the way of 4 neighbors taking priority over 8 neighbors, i.e., if two points in the local structure are already connected by 4 neighbors then they will not be connected by 8 neighbors again,  $\mathcal{G}^{2D} = \{\mathcal{V}^{2D}, \mathcal{E}^{2D}\}$  can be finally obtained.

The results of our rigid registration contain matching relations of the vessel segments  $\pi^{\mathcal{E}}$ , based on which the dense matching of vessel points can be further obtained. However, in practical applications, the registration and matching tasks are not oriented to the same goal. According to Eq. 3, the goal of our MCTS task is to obtain the result with the highest overlap, while its corresponding matching is not necessarily complete. Therefore, we perform another edge matching after rigid registration, consistent with the tree search process, until the maximum number of edge matches  $|\pi^{\mathcal{E}}|$  is reached. Two matching results are shown in Fig. 10, the upper part is the corresponding matching result after rigid registration, and the lower part is the refined maximum matching result. The matching lines are calculated by the dynamic time warping algorithm based on the edge matching. In Fig. 10, the registered 3D vessel projection exhibits good spatial overlap with the 2D vessel. However, for the convenience of displaying the matching lines, we manually applied a translation to the registered 3D vessel projection. The number of matched vascular points is significantly increased after the optimization, which directly contributes to the construction of the deformation model.

## V. DISCUSSION

The rigid registration experiments conducted on simulation data indicate that our method, including our previously proposed topology-based registration methods (GTSR, HTSR, and MCTS), demonstrates strong pose independence. In contrast, other methods exhibit low registration errors within a limited range of angles but experience an increase in error as the rotation angle becomes larger. For nonrigid registration experiments, the Deformable [14], which utilizes a soft version of the matching as proposed by ICP, is highly affected by noise. The Prior [6] solves the point matching problem using the Hungarian algorithm, where the cost function is a linear combination of the Mahalanobis distance between the two points and their similarity in orientation. This correspondence calculation method is also heavily influenced by noise. However, its deformation model was built from synthesized deformations and follows more restrictions, resulting in better performance in terms of registration error compared to Deformable [14]. Both the CAR-Net [7] and our proposed method utilized vessel topology for establishing 3D and 2D vessel matches, making them more robust to noise. The proposed deformation model in our method exhibits better model fitting capability, leading to the minimum registration error.

In 3D/2D registration, foreshortened 2D vessels often lead to significant changes in the length of 3D vessels. However, this phenomenon was not observed in the elastic registration errors shown in Tables III and IV, nor in the examples illustrated in Figures 3, 6, and 8. We believe that the manifold norm  $\|\mathcal{T}\|_{\mathcal{M}}^2$  plays a role here, as it restricts changes in vessel length, a concept reflected in the works [7], [14], [21]. For the foreshortened 2D vessels, the penalty on length changes encourages changes in the direction of the 3D vessels, aligning with real-world scenarios. Of course, none of these methods can completely prevent changes in vessel length, as the objective function of elastic registration also includes the distance error of matched point pairs and the smoothness

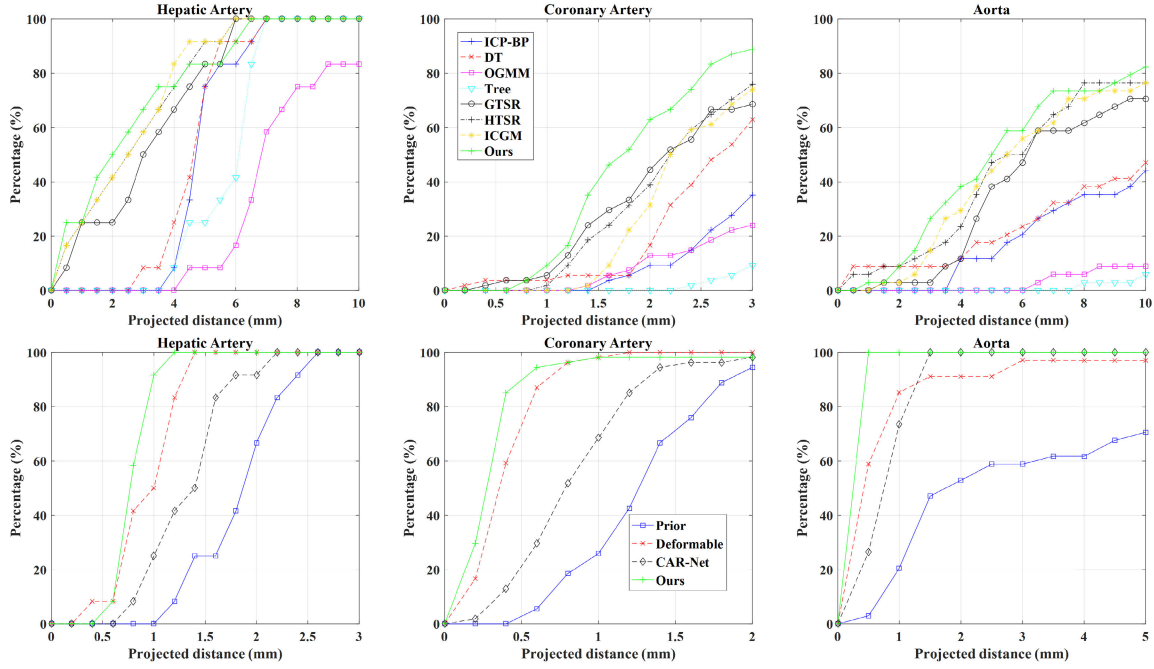


**Fig. 9.** Cumulative histograms of error of 3D/2D rigid and nonrigid registration results on clinical data of hepatic artery, aorta, and coronary arteries. The X-axis denotes mean projected distance with unit of millimeter. The Y-axis denote cumulative percentage of registration error(PD) below a specific value. The first row of histograms represents the results of rigid registration, while the second row of histograms represents the results of nonrigid registration.

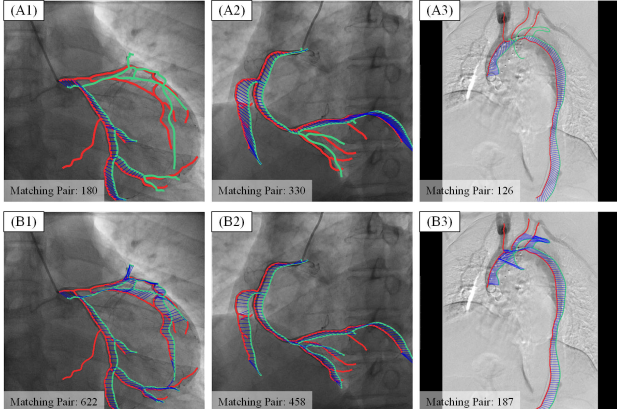


**Fig. 10.** Vessel graph matching. (A1)-(A3): Matching result after rigid registration, (B1)-(B3): the refined maximum matching result. To better visualize the vessel matching lines, we manually applied a translation to the registered 3D vessel projection.

term for the spatial deformation field. The optimal solution is a balance among various penalty terms.

In terms of rigid registration experiments on generated data with computation-induced defects, apart from the Tree method [2], all other approaches exhibit lower registration errors, with our proposed rigid registration method achieving the lowest error. Regarding computational time, the DT method [22], utilizing precomputed distance transforms, averages a mere 0.02 seconds. Conversely, the ICGM method [8], employing graph matching algorithms for vascular point matching, incurs the highest time consumption due to the larger number of nodes in the 2D vascular map. As for nonrigid registration, our method demonstrates a significant advantage in registration error while also exhibiting the lowest time consumption. The Deformable method's [14] method is exceptionally time-consuming because the displacements of

whole 3D points are calculated. While we use several control points for the proposed method to calculate the deformation field, and the matrix formulation in derivative calculation accelerates the computation. The CAR-Net [7] employs a deep learning model to predict deformations in 3D vessels. Despite its higher number of model parameters, which align with the quantity of 3D vascular points, the method still manages to achieve a relatively low computational time. Our nonrigid registration method has an average computation time of 0.51 seconds. Although it outperforms the comparative methods, it has not yet reached the level required to meet the real-time DSA refresh rate of 10-15 frames per second. However, there is still room for improvement in computational efficiency.

Moreover, as illustrated in Table IV, our rigid registration process is more time-intensive compared to our nonrigid registration, which is to be expected. The rigid registration applies the MCTS method, predominantly focused on seeking the best 3D-to-2D vascular match within a defined tree space. Conversely, nonrigid registration adheres to a conventional approach involving the design of objective functions, computation of gradient formulas, and utilization of optimization algorithms to identify the optimal solution proximate to the initial values. It's clear that methods based on tree search are more time-consuming relative to those founded on optimization.

In the case studies depicted in Fig. 8 using manually annotated vascular data, it is evident that the initial poses of all cases exhibit poor alignment with significant rotational differences between the 3D and 2D vessels. This is a challenging problem for optimization-based rigid registration algorithms. However, by employing the MCTS algorithm proposed in this paper, the 3D and 2D vessels achieve improved overlap coverage, and the matching relationship between vessel points is established during the process.

Furthermore, the nonrigid registration algorithm based on manifold regularization is utilized to further enhance vessel overlap. The cumulative histograms presented in Fig. 9 demonstrate that the proposed method achieves the highest accuracy in both rigid and nonrigid registration tests.

Please note that in the comparative experiments of this study, most of the methods used for comparison were reproduced by us. Although we strictly followed the details provided in the authors' papers, we cannot guarantee absolute objectivity in our experiments.

One major limitation of the proposed method is that the topology of vessel centerlines is a mandatory requirement. The errors introduced by the process of generating the topology cannot be avoided to degrade the performance of the registration algorithm. In our simulation experiments, we employed simulated vascular centerlines specifically designed to address DSA vascular noise. This to some extent demonstrates the robustness of our method against noise. However, unlike the simulated data experiments described in the ICGM method, we did not conduct experiments specifically focusing on centerline discontinuities. This is because our methods, including GTSR, HTSR, and Tree, are all based on vascular topology continuity for vessel matching calculations, and centerline discontinuities would significantly impact the matching results. From the vascular segmentation results shown in Fig. 4, it can be observed that discontinuity issues are not prevalent. Deep learning-based methods can utilize strategies such as graph convolutional networks [43] or connectivity supervision [44] to ensure vessel continuity.

Furthermore, for vessels with complex topological structures, such as cerebral vessels, registration algorithms based on vascular topology matching are not applicable. Not only is it challenging to achieve accurate registration results, but the high number of nodes and edges in the vessel graph also leads to excessive time consumption in our rigid registration method. For 3D/2D registration of cerebral vessels, utilizing features derived from intensity or directly using intensity information as a measure for registration is more suitable [45]. Feature-based registration methods have been advantageous for some time because of their faster computational speed, but the disadvantage is that the algorithm for generating features is not perfect. With the upgrading of computing hardware and the development of deep learning technology, it is a possible development direction for 3D/2D registration to use CTA images and DSA images directly without preprocessing for fast and accurate registration, and to use a learning approach to generate directly predictable deformation models instead of iterative deformation model solving process.

Another limitation of this paper is that none of the experiments were conducted on an openly available gold standard dataset. This is because the only such dataset currently available for 3D/2D vascular registration is for cerebral vessels involving CBCT and DSA [46], but our method is not suitable for 3D/2D registration of cerebral vessels. Therefore, we plan to make our code and test data publicly available<sup>1</sup> after the publication of the paper, to enable comparisons by other researchers.

<sup>1</sup>[https://github.com/JianjunZhu/Vessel\\_3D\\_2D\\_Registration](https://github.com/JianjunZhu/Vessel_3D_2D_Registration)

Although our method is designed for 3D/2D registration of vessels, its rigid and nonrigid registration models can be applied to other structures based on topological models. The only constraint is the requirement for weak topological consistency between the 3D and 2D structures, meaning that there exists subgraphs to both the 3D graph  $\tilde{\mathcal{G}}^{3D} \subseteq \mathcal{G}^{3D}$  and 2D graph  $\tilde{\mathcal{G}}^{2D} \subseteq \mathcal{G}^{2D}$ . When the subgraphs are isomorphic  $\tilde{\mathcal{G}}^{3D} \approx \tilde{\mathcal{G}}^{2D}$ , it satisfies the weak consistency requirement for our method.

## VI. CONCLUSION

In this paper, we propose a 3D/2D rigid and nonrigid registration algorithm based on vessel topology. In the rigid task, the topological information is used to construct a vessel matching search tree, a concept first proposed in our previous work [4], [5], which has the advantage that the registration task is converted from an optimal search in parameter space to a tree state search, greatly improving the search efficiency and registration accuracy. In addition, the final rigid registration results of this method can directly obtain dense matching of 3D and 2D vessel points, which is the key to constructing high-quality vascular deformation models. Baka et al. [9] used 4D CT data to construct a statistical shape model to achieve vascular nonrigid registration, and due to the limitation of 4D CT data acquisition, this method is not suitable for clinical applications. Groher et al. [14] used ICP strategy to calculate vascular point matching in their nonrigid registration, which is apparently less accurate than vessel graph matching. Wu et al. [7] used vascular segment-level matching relationships as implicit inputs in their learning-based deformation model. We also used a simulated statistical shape model based on a priori knowledge of coronary deformation to construct deformation model in our previous work [8], and its registration accuracy is not as good as the performance of the proposed method due to the limitations of the model complexity.

Our method is validated on three different vascular anatomies, including the clinical hepatic artery, coronary artery, and aorta. Six rigid and two nonrigid 3D/2D registration methods are compared with our method in the experiments. As the 3D and 2D vessels lack pose initialization before registration, most rigid methods, including ICP-BP, DT, Tree, and OGMM, achieve higher registration error than our method. The GTSR, HTSR, and our method use tree search strategies to achieve registration and can align two data without manual alignment. The manifold regularized deformation model can efficiently warp the 3D vessel to overlap with the 2D vessel. In addition, we discuss the way to construct 3D and 2D vessel graphs, and the calculation method to achieve maximum matching of vessel points.

## ACKNOWLEDGMENT

The funding sources had no role in the writing of the report, or decision to submit the article for publication.

## REFERENCES

- [1] N. Baka, C. T. Metz, C. J. Schultz, R.-J. van Geuns, W. J. Niessen, and T. van Walsum, "Oriented Gaussian mixture models for nonrigid 2D/3D coronary artery registration," *IEEE Trans. Med. Imag.*, vol. 33, no. 5, pp. 1023–1034, May 2014.

- [2] T. Benseghir, G. Malandain, and R. Vaillant, "A tree-topology preserving pairing for 3D/2D registration," *Int. J. Comput. Assist. Radiol. Surg.*, vol. 10, no. 6, pp. 913–923, Jun. 2015.
- [3] S. Liu, P. Liu, Z. Li, Y. Zhang, W. Li, and X. Tang, "A 3D/2D registration of the coronary arteries based on tree topology consistency matching," *Biomed. Signal Process. Control*, vol. 38, pp. 191–199, Sep. 2017.
- [4] J. Zhu et al., "Monte Carlo tree search for 3D/2D registration of vessel graphs," in *Proc. IEEE Int. Conf. Bioinf. Biomed. (BIBM)*, Nov. 2019, pp. 787–791.
- [5] J. Zhu et al., "Heuristic tree searching for pose-independent 3D/2D rigid registration of vessel structures," *Phys. Med. Biol.*, vol. 65, no. 5, Mar. 2020, Art. no. 055010.
- [6] E. Serradell, A. Romero, R. Leta, C. Gatta, and F. Moreno-Noguer, "Simultaneous correspondence and non-rigid 3D reconstruction of the coronary tree from single X-ray images," in *Proc. Int. Conf. Comput. Vis.*, Nov. 2011, pp. 850–857.
- [7] W. Wu, J. Zhang, W. Peng, H. Xie, S. Zhang, and L. Gu, "CAR-Net: A deep learning-based deformation model for 3D/2D coronary artery registration," *IEEE Trans. Med. Imag.*, vol. 41, no. 10, pp. 2715–2727, Oct. 2022.
- [8] J. Zhu et al., "Iterative closest graph matching for non-rigid 3D/2D coronary arteries registration," *Comput. Methods Programs Biomed.*, vol. 199, Feb. 2021, Art. no. 105901.
- [9] N. Baka et al., "Statistical coronary motion models for 2D+t/3D registration of X-ray coronary angiography and CTA," *Med. Image Anal.*, vol. 17, no. 6, pp. 698–709, Aug. 2013.
- [10] M. A. Pinheiro, J. Kybic, and P. Fua, "Geometric graph matching using Monte Carlo tree search," *IEEE Trans. Pattern Anal. Mach. Intell.*, vol. 39, no. 11, pp. 2171–2185, Nov. 2017.
- [11] E. Serradell, J. Kybic, F. Moreno-Noguer, and P. Fua, "Robust elastic 2D/3D geometric graph matching," *Proc. SPIE*, vol. 8314, pp. 82–89, Mar. 2012.
- [12] H. Feuillâtre, J.-C. Nunes, and C. Toumoulin, "An improved graph matching algorithm for the spatio-temporal matching of a coronary artery 3D tree sequence," *IRBM*, vol. 36, no. 6, pp. 329–334, Nov. 2015.
- [13] J. Garcia Guevara, I. Peterlik, M.-O. Berger, and S. Cotin, "Elastic registration based on compliance analysis and biomechanical graph matching," *Ann. Biomed. Eng.*, vol. 48, no. 1, pp. 447–462, Jan. 2020.
- [14] M. Groher, D. Zikic, and N. Navab, "Deformable 2D–3D registration of vascular structures in a one view scenario," *IEEE Trans. Med. Imag.*, vol. 28, no. 6, pp. 847–860, Jun. 2009.
- [15] P. Markelj, D. Tomažević, B. Likar, and F. Pernuš, "A review of 3D/2D registration methods for image-guided interventions," *Med. Image Anal.*, vol. 16, no. 3, pp. 642–661, Apr. 2012.
- [16] A. Varnavas, T. Carrell, and G. Penney, "Fully automated 2D–3D registration and verification," *Med. Image Anal.*, vol. 26, no. 1, pp. 108–119, Dec. 2015.
- [17] S. Miao, R. Liao, J. Lucas, and C. Chefd'Hotel, "Toward accurate and robust 2-D/3-D registration of implant models to single-plane fluoroscopy," in *Augmented Reality Environments for Medical Imaging and Computer-Assisted Interventions*. Cham, Switzerland: Springer, 2013, pp. 97–106.
- [18] A. R. Gouveia, C. Metz, L. Freire, P. Almeida, and S. Klein, "Registration-by-regression of coronary CTA and X-ray angiography," *Comput. Methods Biomech. Biomed. Eng., Imag. Visualizat.*, vol. 5, no. 3, pp. 208–220, May 2017.
- [19] T. F. Cootes, C. J. Taylor, D. H. Cooper, and J. Graham, "Active shape models—their training and application," *Comput. Vis. Image Understand.*, vol. 61, no. 1, pp. 38–59, Jan. 1995.
- [20] K. Rohr, H. S. Stiehl, R. Sprengel, T. M. Buzug, J. Weese, and M. H. Kuhn, "Landmark-based elastic registration using approximating thin-plate splines," *IEEE Trans. Med. Imag.*, vol. 20, no. 6, pp. 526–534, Jun. 2001.
- [21] M. Groher, M. Baust, D. Zikic, and N. Navab, "Monocular deformable model-to-image registration of vascular structures," in *Proc. Int. Workshop Biomed. Image Registration*. Cham, Switzerland: Springer, 2010, pp. 37–47.
- [22] D. Rivest-Henault, H. Sundar, and M. Cheriet, "Nonrigid 2D/3D registration of coronary artery models with live fluoroscopy for guidance of cardiac interventions," *IEEE Trans. Med. Imag.*, vol. 31, no. 8, pp. 1557–1572, Aug. 2012.
- [23] O. M. Dorgham, S. D. Laycock, and M. H. Fisher, "GPU accelerated generation of digitally reconstructed radiographs for 2-D/3-D image registration," *IEEE Trans. Biomed. Eng.*, vol. 59, no. 9, pp. 2594–2603, Sep. 2012.
- [24] E. Kerrien, M.-O. Berger, E. Maurincombe, L. Launay, R. Vaillant, and L. Picard, "Fully automatic 3D/2D subtracted angiography registration," in *Proc. Int. Conf. Med. Image Comput. Comput.-Assist. Intervent.* Cham, Switzerland: Springer, 1999, pp. 664–671.
- [25] J. H. Hipwell et al., "Intensity-based 2-D–3-D registration of cerebral angiograms," *IEEE Trans. Med. Imag.*, vol. 22, no. 11, pp. 1417–1426, Nov. 2003.
- [26] D. Ruijters, B. M. T. Haar Romeny, and P. Suetens, "Vesselness-based 2D–3D registration of the coronary arteries," *Int. J. Comput. Assist. Radiol. Surg.*, vol. 4, no. 4, pp. 391–397, Jun. 2009.
- [27] P. J. Besl and N. D. McKay, "A method for registration of 3-D shapes," *IEEE Trans. Pattern Anal. Mach. Intell.*, vol. 14, no. 2, pp. 239–256, Feb. 1992.
- [28] T. Benseghir, G. Malandain, and R. Vaillant, "Iterative closest curve: A framework for curvilinear structure registration application to 2D/3D coronary arteries registration," in *Proc. Int. Conf. Med. Image Comput. Comput.-Assist. Intervent.* Cham, Switzerland: Springer, 2013, pp. 179–186.
- [29] E. Serradell, M. A. Pinheiro, R. Sznitman, J. Kybic, F. Moreno-Noguer, and P. Fua, "Non-rigid graph registration using active testing search," *IEEE Trans. Pattern Anal. Mach. Intell.*, vol. 37, no. 3, pp. 625–638, Mar. 2015.
- [30] L. Ferraz, X. Binefa, and F. Moreno-Noguer, "Very fast solution to the PnP problem with algebraic outlier rejection," in *Proc. IEEE Conf. Comput. Vis. Pattern Recognit.*, Jun. 2014, pp. 501–508.
- [31] A. Zeng et al., "ImageCAS: A large-scale dataset and benchmark for coronary artery segmentation based on computed tomography angiography images," *Computerized Med. Imag. Graph.*, vol. 109, Oct. 2023, Art. no. 102287.
- [32] W. Liu et al., "Full-resolution network and dual-threshold iteration for retinal vessel and coronary angiograph segmentation," *IEEE J. Biomed. Health Informat.*, vol. 26, no. 9, pp. 4623–4634, Sep. 2022.
- [33] C. Zhao et al., "Automatic extraction and stenosis evaluation of coronary arteries in invasive coronary angiograms," *Comput. Biol. Med.*, vol. 136, Sep. 2021, Art. no. 104667.
- [34] F. Cervantes-Sánchez, I. Cruz-Aceves, A. Hernandez-Aguirre, M. A. Hernandez-Gonzalez, and S. E. Solorio-Meza, "Automatic segmentation of coronary arteries in X-ray angiograms using multiscale analysis and artificial neural networks," *Appl. Sci.*, vol. 9, no. 24, p. 5507, Dec. 2019.
- [35] X. Wang et al., "Automatic labeling of vascular structures with topological constraints via HMM," in *Proc. MICCAI*. Cham, Switzerland: Springer, 2017, pp. 208–215.
- [36] D. Wu et al., "Automated anatomical labeling of coronary arteries via bidirectional tree LSTMs," *Int. J. Comput. Assist. Radiol. Surg.*, vol. 14, no. 2, pp. 271–280, Feb. 2019.
- [37] A. M. Andrew, "Multiple view geometry in computer vision," *Kybernetes*, vol. 30, no. 9, pp. 1333–1341, 2001.
- [38] R. Kress, *Numerical Analysis*, vol. 181. Cham, Switzerland: Springer, 1998.
- [39] A. Sengupta, "Generalized variance," *Encyclopedia Stat. Sci.*, vol. 3, no. 1, pp. 1–12, 2004.
- [40] A. Berlinet and C. Thomas-Agnan, *Reproducing Kernel Hilbert Spaces in Probability and Statistics*. Cham, Switzerland: Springer, 2011.
- [41] R. H. Byrd, P. Lu, J. Nocedal, and C. Zhu, "A limited memory algorithm for bound constrained optimization," *SIAM J. Sci. Comput.*, vol. 16, no. 5, pp. 1190–1208, Sep. 1995.
- [42] E. B. van de Kraats, G. P. Penney, D. Tomazevic, T. van Walsum, and W. J. Niessen, "Standardized evaluation methodology for 2-D–3-D registration," *IEEE Trans. Med. Imag.*, vol. 24, no. 9, pp. 1177–1189, Sep. 2005.
- [43] J. M. Wolterink, T. Leiner, and I. Işgum, "Graph convolutional networks for coronary artery segmentation in cardiac ct angiography," in *Proc. MICCAI*. Cham, Switzerland: Springer, 2019, pp. 62–69.
- [44] M. Kampffmeyer, N. Dong, X. Liang, Y. Zhang, and E. P. Xing, "ConnNet: A long-range relation-aware pixel-connectivity network for salient segmentation," *IEEE Trans. Image Process.*, vol. 28, no. 5, pp. 2518–2529, May 2019.
- [45] U. Mitrović, B. Likar, F. Pernuš, and Ž. Špiclin, "3D–2D registration in endovascular image-guided surgery: Evaluation of state-of-the-art methods on cerebral angiograms," *Int. J. Comput. Assist. Radiol. Surg.*, vol. 13, no. 2, pp. 193–202, Feb. 2018.
- [46] H. Madan, F. Pernuš, B. Likar, and Ž. Špiclin, "A framework for automatic creation of gold-standard rigid 3D–2D registration datasets," *Int. J. Comput. Assist. Radiol. Surg.*, vol. 12, no. 2, pp. 263–275, Feb. 2017.